Int. J. Heat Mass Transfer. Vol. 36, No. 10, pp. 2685–2697, 1993
Printed in Great Britain

0017–9310/93 $6.00 + 0.00

Impinging jet studies for turbulence model assessment—II. An examination of the performance of four turbulence models

T. J. CRAFT, L. J. W. GRAHAM and B. E. LAUNDER
Department of Mechanical Engineering, UMIST, Manchester, U.K.

(*Received* 21 *April* 1992)

Abstract—Four turbulence models are applied to the numerical prediction of the turbulent impinging jets discharged from a circular pipe measured by Cooper *et al.* [*Int. J. Heat Mass Transfer* **36**, 2675–2684 (1993)], Baughn and Shimizu [*ASME J. Heat Transfer* **111**, 1096–1098 (1986)] and Baughn *et al.* [ASME Winter Annual Meeting, November 1992]. They comprise one k–ε eddy viscosity model and three second-moment closures. In the test cases selected, the jet discharge was two and six diameters above a plane surface orthogonal to the jet's axis. The Reynolds numbers were 2.3×10^4 and 7×10^4, the flow being fully developed at the discharge plane. The numerical predictions, obtained with an extended version of the finite-volume TEAM code, indicate that the k–ε model and one of the Reynolds stress models lead to far too large levels of turbulence near the stagnation point. This excessive energy in turn induces much too high heat transfer coefficients and turbulent mixing with the ambient fluid. The other two second-moment closures, adopting new schemes for accounting for the wall's effect on pressure fluctuations, do much better though one of them is clearly superior in accounting for the effects of the height of the jet discharge above the plate. None of the schemes is entirely successful in predicting the effects of Reynolds number. It is our view, however, that the main cause of this failure is the two-equation eddy viscosity scheme adopted in all cases to span the near-wall sublayer rather than the outer layer models on which the present study has focused.

1. INTRODUCTION

IN SOME respects CFD for turbulent flows can already be said to be a mature subject. Numerical algorithms are sufficiently refined and computational power sufficiently abundant that in two-dimensional and even some three-dimensional flows purely numerical errors can be reduced to insignificant levels. A sign of this advancing maturity is the growth in the use of commercial CFD software that is seemingly able to solve, in a routine way, any fluid flow problem that may arise. The reality, however, is that no software can be better than the physical models embedded within it. The models of turbulent mixing incorporated in these codes are, for the most part, ones developed twenty years or so ago at a time when computer limitations meant that the empirical coefficients they contain had to be tuned by reference to simple thin shear flows.

The impinging turbulent axisymmetric jet on which attention is here focused provides a strikingly different test flow: the motion in the vicinity of the stagnation point comprises a nearly irrotational normal straining (rather than simple shearing), while that nearer the edge of the impinging jet combines strong rotationality and streamline curvature. Finally, further from the impingement point the flow does revert to a thin shear flow but by no means to a simple one, with the maximum shear stress occurring outside the wall region and the flow thus retaining a significant memory of its upstream history. Because the flow is geometrically simple, it can be easily handled from a numerical point of view. It thus provides an ideal test case for turbulence model assessment. In the present contribution, four models have been tested. Two of these have been very widely used in research and in commercial software: the low-Reynolds-number k–ε eddy viscosity model of Launder and Sharma [1] and the basic second-moment closure of Gibson and Launder [2]. Two new schemes have also been considered where one of the impinging jet flows has been used to help calibrate the sub-model relating to wall effects on the pressure-strain process.

The turbulence models are presented in Section 2 together with relevant details concerning the solver and the numerical computations. The results are discussed in relation to the experimental data in Section 3.

2. THE COMPUTATIONAL PROGRAMME

2.1. *The models considered*

The four models tested are detailed in Tables 1–4. Model 1, summarized in Table 1, is the low-Reynolds-number k–ε model of Launder and Sharma [1] with the so-called 'Yap correction' added to the transport equation for $\tilde{\varepsilon}$ [3]. This scheme is also adopted across the low-Reynolds-number sublayer in the case of Models 2–4 since they are held to apply only where viscous effects are negligible. These models are all second-moment closures where the turbulent stresses $\overline{u_i u_j}$ form the subject of differential transport equa-

NOMENCLATURE

a_{ij}	anisotropic stress, $\overline{u_iu_j}/k-\frac{2}{3}\delta_{ij}$	T	mean temperature
A	stress invariant, $1-9/8(A_2-A_3)$	T_w	wall temperature
A_2	stress invariant, $a_{ij}a_{ij}$	$\overline{u_iu_j}$, $\overline{u^2}$, $\overline{v^2}$, $\overline{w^2}$, $\overline{uv}$	Reynolds stresses
A_3	stress invariant, $a_{ij}a_{jk}a_{ki}$	$\overline{u_i\theta}$	heat flux
d_{ij}	diffusion of Reynolds stress	u', v'	r.m.s. fluctuating velocities
d_k	diffusion of turbulence energy	U_i, U, V	mean velocity components
$d_{i\theta}$	diffusion of heat flux	U_B	bulk velocity
d_θ	diffusion of scalar variance	x_i	coordinate direction
D	diameter of inlet pipe	y	distance from wall
D_{ij}	tensor used in new stress models	Y_c	Yap correction.
f_ε, f_μ	damping functions in k–ε model		
f_y	length-scale function		
H	height of jet discharge above plate	Greek symbols	
k	turbulent kinetic energy	δ_{ij}	Kronecker delta
n_i	component of unit vector normal to wall	ε	dissipation rate of k
Nu	Nusselt number	$\tilde{\varepsilon}$	isotropic dissipation rate of k
Pr	Prandtl number	ε_{ij}	dissipation rate of Reynolds stress
P_{ij}	Reynolds stress generation rate	$\varepsilon_{i\theta}$	dissipation rate of heat flux
P_k	turbulence energy generation rate	ε_θ	dissipation rate of scalar variance
$P_{i\theta}$	heat flux generation rate	$\overline{\theta^2}$	scalar variance
P_θ	scalar variance generation rate	ν	kinematic viscosity
r	radial distance	ν_t	turbulent viscosity
R	time-scale ratio	σ_θ	turbulent Prandtl number
Re	bulk Reynolds number	ϕ_{ij}	pressure–strain correlation
R_t	turbulent Reynolds number	$\phi_{i\theta}$	pressure–scalar gradient correlation.

Table 1. Low Reynolds number k–ε model

$$\frac{Dk}{Dt} = d_k + P_k - \varepsilon$$

$$\frac{D\tilde{\varepsilon}}{Dt} = c_{\varepsilon 1}\frac{\tilde{\varepsilon}\nu_t}{k}\left(\frac{\partial U_i}{\partial x_j}+\frac{\partial U_j}{\partial x_i}\right)\frac{\partial U_i}{\partial x_j} - c_{\varepsilon 2}f_\varepsilon\frac{\tilde{\varepsilon}^2}{k} + 2\nu\nu_t\left(\frac{\partial^2 U_i}{\partial x_j\partial x_k}\right)^2 + \frac{\partial}{\partial x_j}\left[\left(\nu+\frac{\nu_t}{\sigma_\varepsilon}\right)\frac{\partial\tilde{\varepsilon}}{\partial x_j}\right] + Y_c$$

$$\overline{u_i\theta} = -\frac{\nu_t}{\sigma_\theta}\frac{\partial T}{\partial x_i}$$

$$d_k = \frac{\partial}{\partial x_j}\left[\left(\nu+\frac{\nu_t}{\sigma_k}\right)\frac{\partial k}{\partial x_j}\right]$$

$$P_k = \nu_t\left(\frac{\partial U_i}{\partial x_j}+\frac{\partial U_j}{\partial x_i}\right)\frac{\partial U_i}{\partial x_j}$$

$$Y_c = c_w\left(\frac{k^{3/2}}{c_1\tilde{\varepsilon}y}-1\right)\left(\frac{k^{3/2}}{c_1\tilde{\varepsilon}y}\right)^2\frac{\tilde{\varepsilon}^2}{k} \quad \text{(Yap correction)}$$

$$\varepsilon = \tilde{\varepsilon}+2\nu\left(\frac{\partial k^{1/2}}{\partial x_j}\right)^2$$

$$\nu_t = c_\mu f_\mu k^2/\tilde{\varepsilon}$$

$$f_\mu = \exp\left\{-\frac{3.4}{(1+R_t/50)^2}\right\}$$

$$f_\varepsilon = (1-0.3\exp\{-R_t^2\})$$

$$R_t = \frac{k^2}{\nu\tilde{\varepsilon}}$$

$$c_{\varepsilon 1}=1.44 \quad c_{\varepsilon 2}=1.92 \quad c_\mu=0.09 \quad c_w=0.83 \quad c_l=2.5$$
$$\sigma_k=1.0 \quad \sigma_\varepsilon=1.3 \quad \sigma_\theta=0.9$$

Table 2. Basic Reynolds stress model, Model 2

$$\phi_{ij} = \phi_{ij1} + \phi_{ij2} + \phi^{w}_{ij1} + \phi^{w}_{ij2}$$

$$\phi_{ij1} = -c_1 \frac{\varepsilon}{k}(\overline{u_i u_j} - \tfrac{2}{3}k\delta_{ij})$$

$$\phi_{ij2} = -c_2(P_{ij} - \tfrac{1}{3}P_{kk}\delta_{ij})$$

$$\phi^{w}_{ij1} = c_{1w}\frac{\varepsilon}{k}(\overline{u_m u_l} n_m n_l \delta_{ij} - \tfrac{3}{2}\overline{u_i u_m} n_m n_j - \tfrac{3}{2}\overline{u_j u_m} n_m n_i) f_y$$

$$\phi^{w}_{ij2} = c_{2w}(\phi_{ml2} n_m n_l \delta_{ij} - \tfrac{3}{2}\phi_{im2} n_m n_j - \tfrac{3}{2}\phi_{jm2} n_m n_i) f_y$$

$$f_y = k^{3/2}/(c_l \varepsilon y)$$

$$H_\varepsilon = c_{\varepsilon 1}\frac{\varepsilon}{k}P_k - c_{\varepsilon 2}\frac{\varepsilon^2}{k}$$

$c_1 = 1.8 \quad c_2 = 0.6 \quad c_{1w} = 0.5 \quad c_{2w} = 0.3$
$c_{\varepsilon 1} = 1.44 \quad c_{\varepsilon 2} = 1.92 \quad c_\varepsilon = 0.18 \quad c_l = 2.5$

tions that may be written:

$$\frac{D\overline{u_i u_j}}{Dt} = d_{ij} + P_{ij} + \phi_{ij} - \varepsilon_{ij}. \tag{1}$$

The shear generation

$$P_{ij} \equiv -\left\{\overline{u_i u_k}\frac{\partial U_j}{\partial x_k} + \overline{u_j u_k}\frac{\partial U_i}{\partial x_k}\right\}$$

requires no approximation and the same model is adopted in all cases for d_{ij} and ε_{ij}, namely:

$$d_{ij} \equiv \frac{\partial}{\partial x_k}\left(c_s \overline{u_i u_k}\frac{k}{\varepsilon}\frac{\partial \overline{u_i u_j}}{\partial x_l}\right)$$

and

$$\varepsilon_{ij} \equiv \tfrac{2}{3}\delta_{ij}\varepsilon.$$

As usual the pressure–strain process ϕ_{ij} is decomposed into a non-linear, turbulent part, ϕ_{ij1}, a mean shear (or 'rapid') part, ϕ_{ij2}, and a wall-reflection contribution, ϕ^{w}_{ij}. Finally, as with the k–ε model, the energy dissipation rate is obtained from its own transport equation

$$\frac{D\varepsilon}{Dt} = H(\varepsilon) + \frac{\partial}{\partial x_k}\left(c_\varepsilon \overline{u_l u_k}\frac{k}{\varepsilon}\frac{\partial \varepsilon}{\partial x_l}\right). \tag{2}$$

The three models differ in their approximation of ϕ_{ij} and $H(\varepsilon)$. Table 2 gives the Basic Model that has figured in very many computations and been incorporated in several commercial CFD codes; Table 3 presents the replacement form of ϕ^{w}_{ij} that Craft and Launder [4] proposed in the light of their initial experience in predicting impinging flows with the Basic Model. It is the term with coefficient c''_{2w} that ensures that, in an impinging flow, there is an appropriately large energy transfer rate from the fluctuating velocity normal to the wall. In simple shear that contribution is negligible and the term as a whole functions much as the superseded version of ref. [2]. Table 4 sets out the more elaborate scheme that, over a three-year period of testing at UMIST, had performed rather encouragingly in free flows, [5] and in an impinging jet at $H/D = 2.0$ at one Reynolds number [6].

To compute the heat transfer coefficients along the impingement surface requires, in the case of the second-moment closures, the solution of transport equations for the turbulent heat fluxes. Paradoxically, the model for the heat fluxes has only a very secondary effect on the heat transfer coefficient in the present test case and for this reason the form for each of the schemes is deferred to the Appendix. The reason, as we shall later see, is that in the near-impingement region most of the temperature drop occurs across the low Reynolds number sublayer. The most important factor in determining the local Nusselt number is thus the distribution of turbulent heat flux across the sublayer or, since a k–ε model is used in this region, the distribution of turbulent thermal diffusivity. In the present study the thermal diffusivity across the sublayer is prescribed via the turbulent Prandtl number, σ_θ, (Table 1); a uniform value of 0.9 has been assigned to this quantity in common with the majority of computations made with this model. The above remarks do not mean that the wall heat transfer coefficient is virtually independent of the outer layer

Table 3. New wall-reflection model, Model 3

As Model 2 except:

$$\phi^{w}_{ij1} = c_{1w}\frac{\varepsilon}{k}(\overline{u_m u_l} n_m n_l \delta_{ij} - \tfrac{3}{2}\overline{u_i u_m} n_m n_j - \tfrac{3}{2}\overline{u_j u_m} n_m n_i) f_y$$

$$\phi^{w}_{ij2} = -c_{2w}\frac{\partial U_l}{\partial x_m}\overline{u_i u_m}(n_q n_q \delta_{ij} - 3n_i n_j) f_y - c'_{2w} k\left(\frac{\partial U_k}{\partial x_m} n_l n_k a_{lm}\delta_{ij} - \frac{3}{2}\frac{\partial U_i}{\partial x_m} n_l n_j a_{lm} - \frac{3}{2}\frac{\partial U_j}{\partial x_m} n_l n_i a_{lm}\right) f_y$$
$$+ c''_{2w} k \frac{\partial U_l}{\partial x_m} n_l n_m (n_l n_j - \tfrac{1}{3} n_q n_q \delta_{ij}) f_y$$

$$f_y = k^{3/2}/(c_l \varepsilon y)$$

$c_{1w} = 0.5 \quad c_{2w} = 0.08 \quad c'_{2w} = 0.1 \quad c''_{2w} = 0.4 \quad c_l = 2.5$

Table 4. New Reynolds stress model, Model 4

$$\phi_{ij} = \phi_{ij1} + \phi_{ij2} + \phi_{ij}^{w}$$

$$\phi_{ij1} = -c_1\varepsilon(a_{ij} + c_1'(a_{ik}a_{jk} - \tfrac{1}{3}A_2\delta_{ij})) - \varepsilon a_{ij}$$

$$\phi_{ij2} = -0.6(P_{ij} - \tfrac{1}{3}\delta_{ij}P_{kk}) + 0.3\varepsilon a_{ij}(P_{kk}/\varepsilon)$$
$$-0.2\left[\frac{\overline{u_k u_j}\,\overline{u_l u_i}}{k}\left(\frac{\partial U_k}{\partial x_l} + \frac{\partial U_l}{\partial x_k}\right) - \frac{\overline{u_l u_k}}{k}\left(\overline{u_i u_k}\frac{\partial U_j}{\partial x_l} + \overline{u_j u_k}\frac{\partial U_i}{\partial x_l}\right)\right]$$
$$-0.6[A_2(P_{ij} - D_{ij}) + 3a_{mi}a_{nj}(P_{mn} - D_{mn})]$$

$$\phi_{ij}^{w} = -c_{2w}\frac{\partial U_l}{\partial x_m}\overline{u_l u_m}(n_q n_q\delta_{ij} - 3n_i n_j)f_y$$
$$-c_{2w}'k\left(\frac{\partial U_k}{\partial x_m}n_l n_k a_{lm}\delta_{ij} - \frac{3}{2}\frac{\partial U_i}{\partial x_m}n_l n_j a_{lm} - \frac{3}{2}\frac{\partial U_j}{\partial x_m}n_l n_i a_{lm}\right)f_y$$
$$+c_{2w}''k\frac{\partial U_l}{\partial x_m}n_l n_m(n_i n_j - \tfrac{1}{3}n_q n_q\delta_{ij})f_y$$

$$D_{ij} = -\left(\overline{u_i u_k}\frac{\partial U_k}{\partial x_j} + \overline{u_j u_k}\frac{\partial U_k}{\partial x_l}\right)$$

$$f_y = k^{3/2}/(c_l\varepsilon y)$$

$$H_\varepsilon = c_{\varepsilon 1}\frac{\varepsilon}{k}\left[P_k + \nu_t\left(\frac{\partial U_i}{\partial x_j}\right)^2\right] - c_{\varepsilon 2}\frac{\varepsilon^2}{k}$$

$$\nu_t = 0.09\frac{k^2}{\varepsilon}$$

$$c_1 = 3.1(A_2A)^{1/2} \quad c_1' = 1.2 \quad c_{2w} = 0.044 \quad c_{2w}' = 0.08 \quad c_{2w}'' = 0.6$$
$$c_{\varepsilon 1} = 0.35 \quad c_{\varepsilon 2} = 1.92/(1 + 1.65A_2^{1/2}A) \quad c_\varepsilon = 0.18 \quad c_l = 2.5$$

turbulence model. The wall heat transfer coefficient depends quite sensitively on the level of turbulence energy prevailing near the edge of the fully turbulent region and this is, of course, determined by the model for the turbulent stresses in the outer layer.

2.2. *The numerical solver*

Computations were made with a specially developed version of the TEAM computer program [7]. This solver is based on a finite-volume solution of the elliptic mean momentum, energy and turbulent transport equations. It adopts a staggered mesh and the Patankar–Spalding [8] SIMPLE algorithm for successively correcting the pressure field to secure compliance with continuity. In using the second-moment closure, the second moments were located in space so that they lay on the control-volume boundaries of the mean velocity component on which they acted; likewise, the heat-flux nodes were placed on the boundaries of the temperature control volume that are orthogonal to the direction of the heat flux.

In the computations reported below, convective transport in the mean flow variables has been approximated via the third order quadratic upwind scheme, QUICK [9]. Craft [10] has carried out an extensive grid refinement study for the impinging jet and found no perceptible change in the computed results from refining the mesh from 80×70 to 100×90 when the QUICK scheme was adopted (with this somewhat more refined mesh the nodes were redistributed so that the internode spacings in the most critical regions were at least halved). By contrast, significant grid sensitivity was suggested from trial computations made with the first-order power-law differencing scheme (PLDS). An 80 (normal to the plate) $\times 70$ (radial) grid has thus been adopted for the majority of computations reported in Section 3 for the case $H/D = 2.0$. Twenty-eight of the 80 nodes covered the low-Re sublayer while in the radial direction nodes were concentrated in the region $r = D/2$ to resolve accurately the mixing layer springing from the jet discharge. For $H/D = 6$ initial computations were made with a 120×70 grid. Further exploration suggested, however, that with an optimally distributed grid a 90×70 mesh was sufficient. For both H/D ratios, as the pipe Reynolds number was increased the near-wall concentration of nodes was increased so that the internode spacing in terms of wall units remained approximately the same as for $Re = 23\,000$.

2.3. *Boundary and compatibility conditions*

The boundary conditions are summarized in Fig. 1. At the jet discharge the flow is fully developed. Accordingly, a separate computation was made of developing flow in a pipe with the parabolic (marching) solver PASSABLE [11] that was continued downstream until fully developed conditions were reached. The turbulence model adopted was the Basic Model

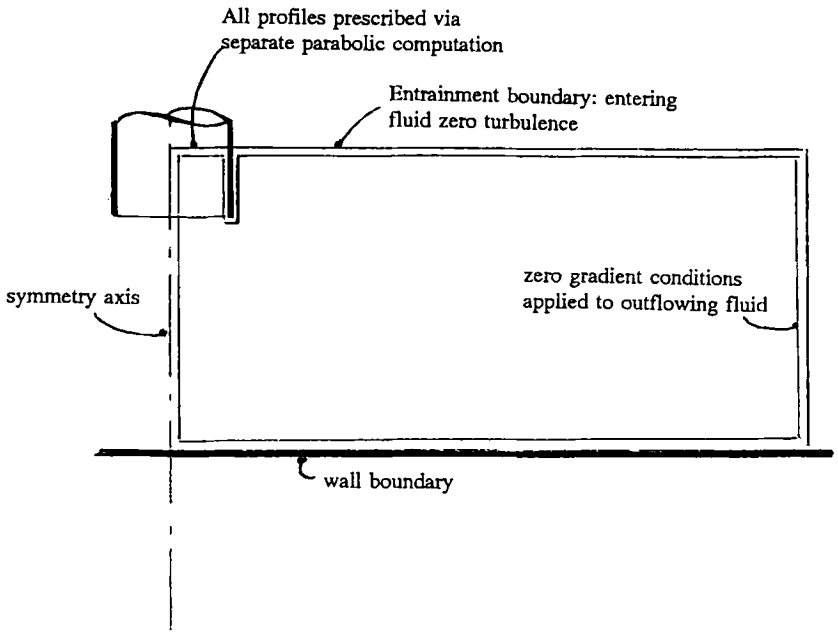

FIG. 1. The solution domain and a summary of the boundary conditions.

(given in Table 2). The computed mean velocity, Reynolds stress and dissipation profiles obtained in this preliminary calculation were interpolated on to the portion of the mesh for the impinging jet calculation covering the pipe inlet. In fact, as indicated in Fig. 1, the inlet section was actually taken at 0.5 jet diameters above the end of the pipe for stability reasons. Over the remainder of the upper boundary and at the right hand outflow boundary the static pressure was treated as uniform which enabled the velocity normal to the boundary to be obtained from continuity. The constraint on the turbulence variables along these boundaries depended on whether the flow was entering or leaving the domain. In-flowing fluid was assigned zero values of turbulent stress and dissipation while, for fluid leaving, zero gradient values were applied.

On the left hand axis of symmetry, zero-gradient

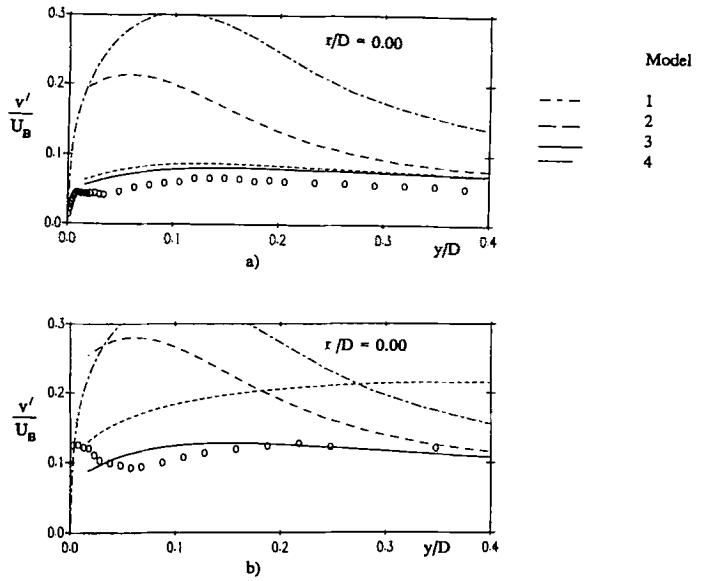

FIG. 2. Root-mean-square turbulent velocity normal to wall on stagnation line, $Re = 23000$. (a) $H/D = 2$; (b) $H/D = 6$.

values were assigned to all variables except the radial velocity U, the shear stress $\overline{uv}$ and heat flux $\overline{u\theta}$ whose values were set to zero. Finally on the wall the radial and normal velocity components were set to zero as were the turbulence energy k and the quasi-dissipation $\tilde{\varepsilon}$ (the dissipation itself is $\tilde{\varepsilon}+2\nu(\partial k^{1/2}/\partial y)^2$ and is non-zero at the wall). A uniform temperature gradient was applied along the wall corresponding to the constant heat flux of the experiments.

The interface between the regions adopting a second-moment closure and the eddy viscosity model was fixed along a single radial line at a distance from the wall such that the average turbulent Reynolds number R_t there was about 150. At the interface continuity of shear stress, heat flux, temperature, turbulent kinetic energy and ε was enforced. Because eddy viscosity schemes return such highly inaccurate values of normal stresses, however, it was seen as counterproductive to impose these inaccurate values of $\bar{u}^2$, $\bar{v}^2$ and $\bar{w}^2$ implied by the k–ε model on the outer-region turbulence model. Instead, gradients of $\overline{u^2}/k$ etc. were set to zero at the inner boundary of the region handled by second moment closure. In practice, this weak constraint should be satisfactory since it exerts an influence only on the diffusive transport across the interface where, in any event, generation and dissipation agencies are much more influential than diffusion in the stress budgets.

3. PRESENTATION AND DISCUSSION OF RESULTS

A powerful impression of the strengths and weaknesses of the different turbulence models in handling stagnation flows is provided by Fig. 2. This shows the distribution of the normalized r.m.s. turbulent velocity normal to the wall along the jet symmetry axis. The k–ε scheme, Model 1, produces excessive turbulence energies and this leads to levels of v' up to four times as large as in the experiment. This very poor prediction arises mainly from the use of the eddy-viscosity stress–strain law to represent normal stresses,

$$\left(\overline{v^2} = \tfrac{2}{3}k - 2\nu_t \frac{\partial V}{\partial y}\right), \quad \text{etc.}$$

which leads to a turbulence energy generation rate in the irrotational region close to the stagnation point of

$$3\nu_t\left(\frac{\partial V}{\partial y}\right)^2.$$

As the turbulence energy becomes too large so does ν_t which further serves to amplify k.

What is perhaps initially surprising is that the basic second-moment closure, Model 2, does not do much better. The culprit in this case is the model of the process ϕ^w_{ij2}. This wall correction principally reduces the strength of the process ϕ_{ij2} when the suffices i or j denote the direction normal to the wall. In a simple shear flow the action of ϕ_{ij2} is to transfer a proportion of the energy generated in streamwise fluctuations to those in the plane orthogonal to the mean velocity; thus the intervention of ϕ^w_{ij2} reduces the effective generation rate of $\overline{v^2}$; its level is therefore lower than in a free flow. In the present stagnation flow, however, the principal stress generation is in the $\overline{v^2}$ component itself. The process ϕ_{ij2} would normally export a large proportion of this generation to other components but this transfer is reduced by ϕ^w_{ij2}. Thus, in a stagnation flow the wall 'damping' term ϕ^w_{ij2} actually leads to an *augmentation* of the turbulent velocity normal to the wall.

The other two Reynolds stress models (Models 3 and 4) both give very much closer agreement with the measured data at $H/D = 2.0$. This is not surprising since *their* wall corrections have been developed with this particular test case in mind [4, 6]. It is interesting to note that the increase in H/D from 2.0 to 6.0 roughly doubles the near-wall turbulent velocity levels, a trend that is well captured by Model 3 but not by Model 4. The excessive near-wall energy that the latter scheme predicts derives from a recently discovered weakness of this model in the developing-flow region of jets: the reduced importance of mean strain in the dissipation equation adopted by this scheme (cf Table 4 and 2) leads to a too slow rise in ε and thus to an appreciable overshoot in Reynolds stress levels (El Baz [12]).

The mean velocity in the stagnation region is pressure dominated and not significantly affected by Reynolds stresses. We note, however, that if (as proposed in ref. [13]) the recorded mean velocity of the single hot wire on the axis is interpreted as $\sqrt{(V^2+\overline{v^2}+\overline{u^2})}$, Fig. 3, the predicted profile with Model 3 for $H/D = 6$ accords quite well with the experimental data with, in particular, the strongly non-linear variation very close to the wall being well captured. Model 1 and, to a lesser extent, Model 2 produce too high near-wall velocities because the turbulence levels they predict are excessive. Model 4 gives too low velocities because of the excessive mixing of the jet *before* coming under the influence of the wall.

The development of the mean and fluctuating velocities as the flow develops away from the stagnation point is presented in Figs. 4–7 for $H/D = 2.0$. The

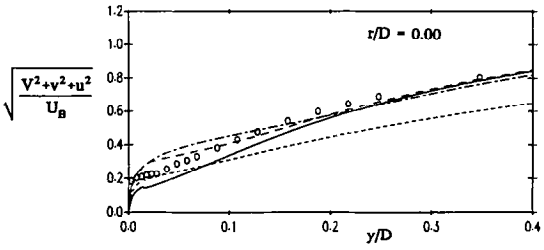

FIG. 3. Variation of 'apparent' mean velocity normal to plate on stagnation line. $H/D = 6$; $Re = 23\,000$. Key as Fig. 2.

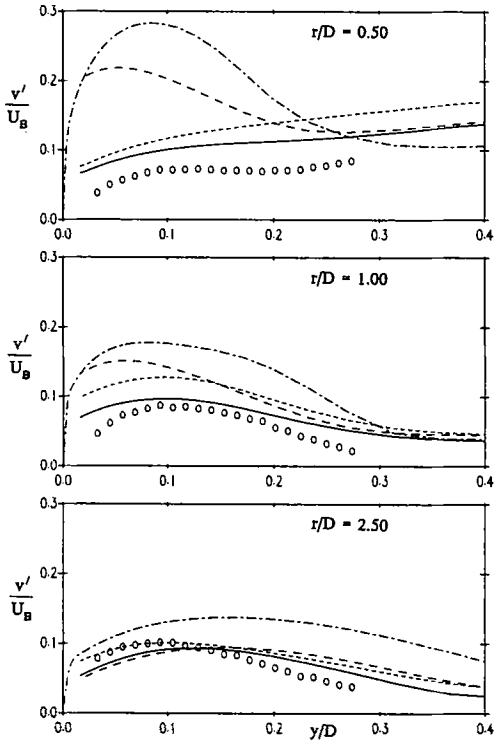

FIG. 4. Development of v' with radius. $H/D = 2.0$; $Re = 23\,000$. Key as Fig. 2.

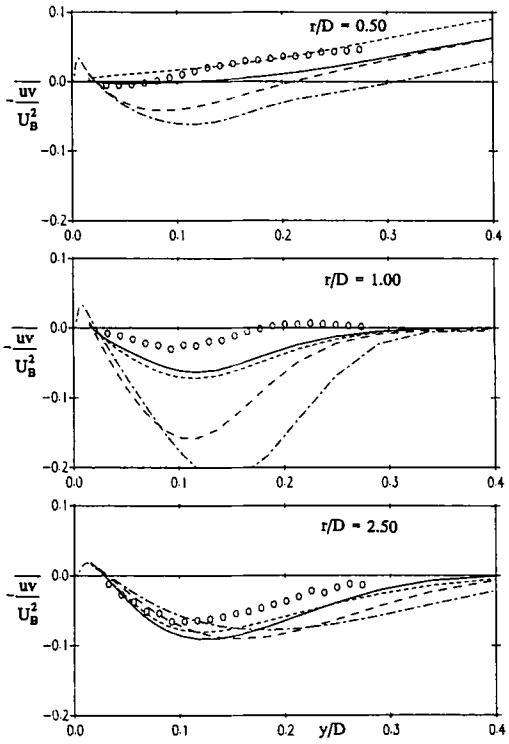

FIG. 6. Turbulent shear stress profiles in the radial wall jet. $H/D = 2.0$; $Re = 23\,000$. Key as Fig. 2.

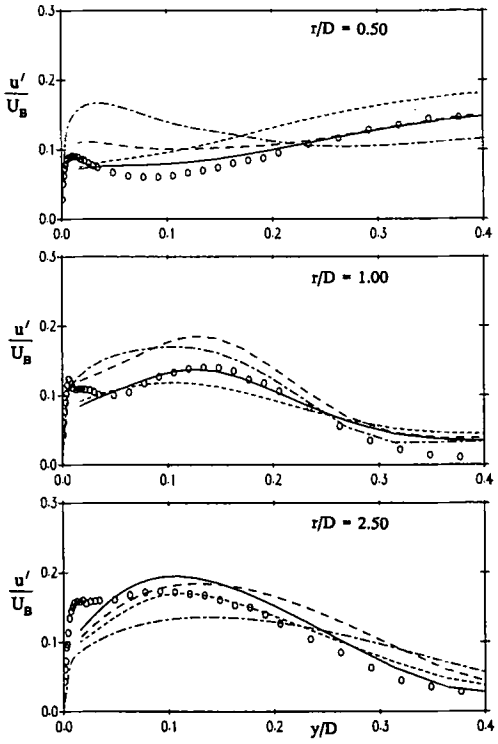

FIG. 5. Development of r.m.s. velocity fluctuations in direction of mean velocity vector. $H/D = 2.0$; $Re = 23\,000$. Key as Fig. 2.

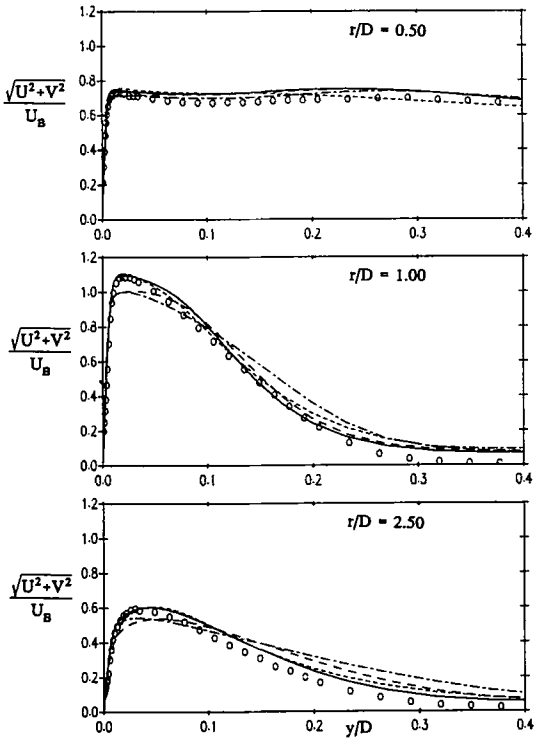

FIG. 7. Development of mean velocity profile in radial wall jet. $H/D = 2.0$; $Re = 23\,000$. Key as Fig. 2.

pattern displayed in Fig. 2(a) is largely reproduced at greater radial distances, Fig. 4, even though, as shear replaces normal straining as the principal energy-generation agency, the weaknesses of Models 1 and 2 identified above are not as important. At $r/D = 2.5$, Model 1 gives particularly high levels of v' at large y/D even though (as we shall see in Fig. 7) the predicted mean velocity gradients are weaker than in the experiment. This appears to be due principally to the insensitivity of eddy viscosity models to the effects of streamline curvature. By contrast, the three second-moment closures give fairly similar results to one another with appreciably lower levels of v'. Note that, in Fig. 5 the computed quantity presented as u' is actually the r.m.s. fluctuating velocity in the direction of the mean velocity vector, for it is believed that this is what the single wire velocity data will have recorded. (In fact only at $r/D = 0.5$ for values of y/D greater than 0.1 does the plotted quantity differ significantly from the r.m.s. radial velocity.) Again Model 3, followed by 4, gives the most accurate account of the development, with Models 1 and 2 being less successful—though not as spectacularly so as for v'. The same relative pattern is evident in the shear–stress comparisons presented in Fig. 6. Finally, so far as $H/D = 2.0$ is concerned, the mean velocity profiles in Fig. 7 serve to confirm the impressions formed from the fluctuating velocity field. Models 3 and 4 achieve close correspondence with the measurements whereas Models 1 and 2 produce too rapid mixing as would be expected from the excessive predicted levels of shear stress shown in Fig. 6.

The computations of the velocity field show virtually no effect of Reynolds number and for this reason the results at $Re = 77000$ have not been included. At this higher flow rate the level of agreement between Model 3 and the data is on the whole slightly better than at $Re = 23000$ as the experiments themselves *do* show a weak influence of Re.

The computations for the jet placed six diameters above the impingement surface are shown in Figs. 8–10 for the higher jet Reynolds number. (The results at $Re = 23000$ display a similar behaviour, though since the experiments in this case are limited to mean velocity and u', comparisons at the higher Re have been selected.) The profiles of streamwise and normal turbulent velocities are shown at three stations in Fig. 8. The general picture to emerge is very similar to that at $H/D = 2$. One notes the excessive levels of v' near the stagnation point ($r/D = 0.5$) returned by Models 1 and 2 and the relatively small differences among the models in predicting u'. As at $H/D = 2.0$, none of the models captures the near-wall peak of u' found in the measurements, a discrepancy that is believed to arise

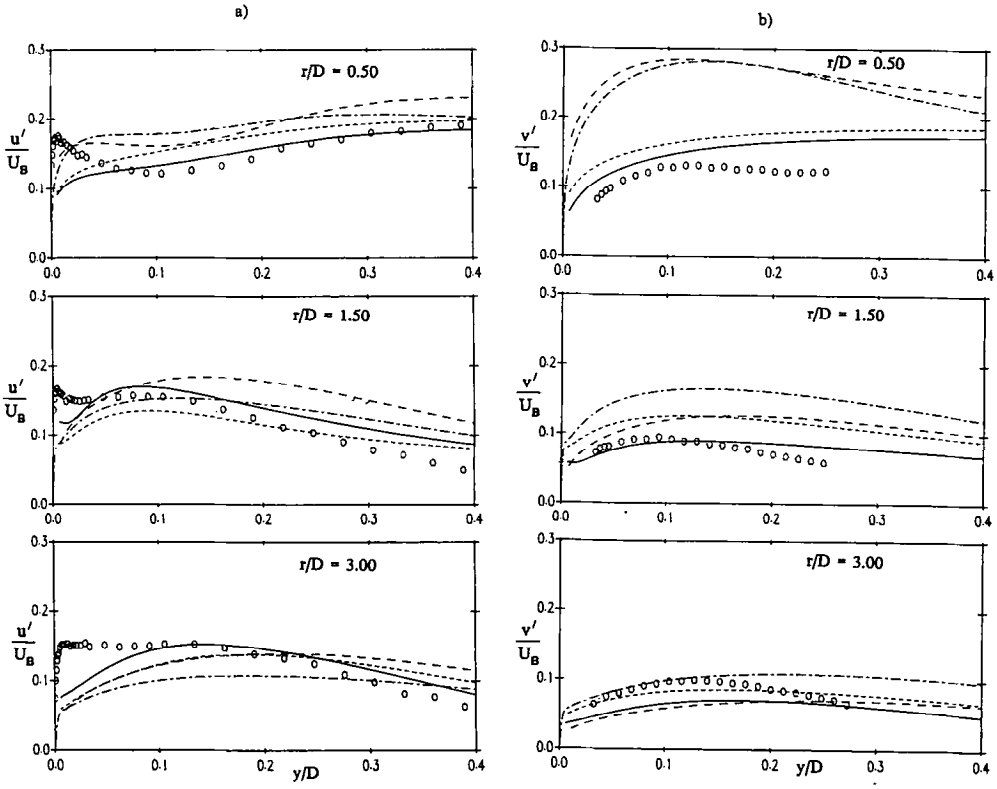

FIG. 8. Profiles of r.m.s. turbulent velocity in radial wall jet. $H/D = 6.0$; $Re = 70000$. Key as Fig. 2. (a) Component parallel to wall; (b) Component normal to wall.

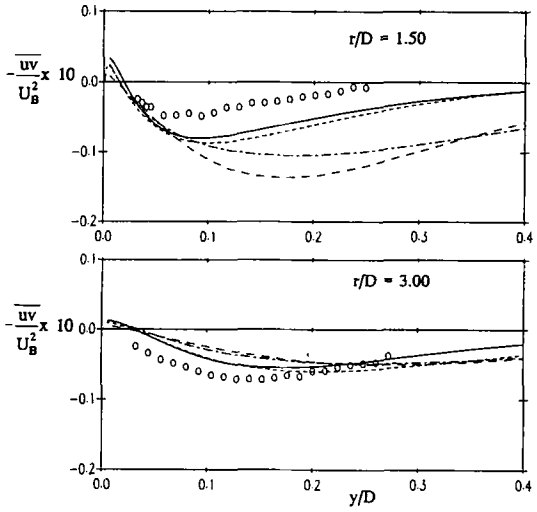

FIG. 9. Development of turbulent shear stress in radial wall jet. $H/D = 6.0$; $Re = 70\,000$. Key as Fig. 2.

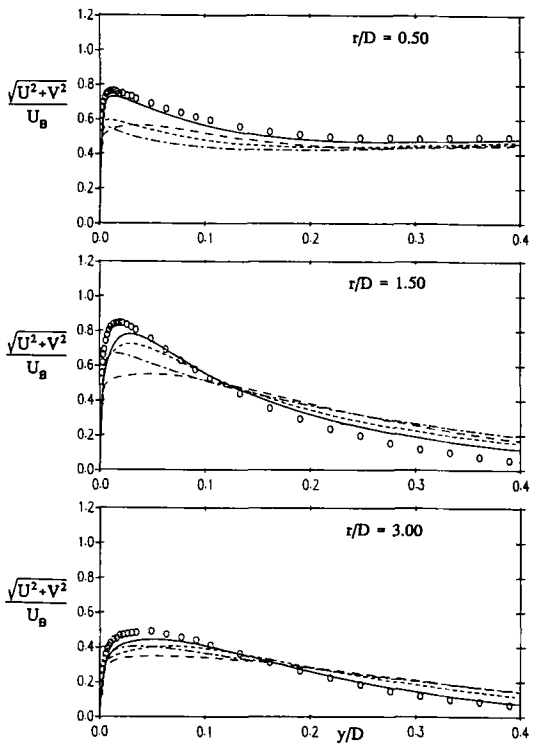

FIG. 10. Mean velocity profiles in radial wall jet. $H/D = 6.0$; $Re = 70\,000$. Key as Fig. 2.

from the use of the k–ε eddy viscosity model across the sublayer.† Overall, Model 3, followed by Model 4, achieves the best agreement though by $r/D = 3.0$, the predicted levels of both the fluctuating velocities given by all the second moment closures are somewhat too low. A similar pattern may be seen in the shear-stress data of Fig. 9. The resultant mean velocity profiles are compared with the experimental data in Fig. 10. All the models produce somewhat too rapid mixing initially, leading to a peak velocity at $r/D = 1.5$ lower than measured and too high velocities in the outer part of the wall jet. The discrepancy is plainly least for Model 3 which is in line with the Reynolds stress data. Apart from the superiority of Model 3 the relative agreement achieved with the other models changes from station to station and in a way that does not always seem consistent with the $\overline{uv}$ profiles. The reason for this apparent inconsistency is that, unlike the case of a thin shear layer, the normal stress terms make a substantial contribution to the mean momentum budget for $r/D < 1.5$. The different models predict very different levels of $(\overline{u^2}-\overline{v^2})$ and the radial gradient of this quantity is effectively a source in the radial momentum equation.

The final comparisons are with the Nusselt number data of Baughn and Shimizu [14] and Baughn *et al.* [15]. Figure 11 considers impingement at $H/D = 2.0$ for two Reynolds numbers. As with the dynamic field, the results predicted by the four models group themselves in pairs: Models 1 and 2 produce excessive levels of Nusselt number due, we suggest, to the far too high turbulence energy near the stagnation point while Models 3 and 4 do rather better, predicting at least qualitatively the increase in Nusselt number with radius that occurs in the range $1.2 < r/D < 2.0$. These last two schemes also capture the dependence of Nusselt number on the Reynolds number at the stagnation point better than Models 1 and 2. The reason for this is that, with the turbulence energy levels being much lower for Models 3 and 4, the thermal boundary layer at the stagnation point is virtually confined within the viscous sublayer, Fig. 12; thus, like the data, the dependence of Nusselt number on Reynolds number is close to the 0.5 power found in laminar flow. Beyond $r/D = 2.0$, both experiments and computations indicate that Nu rises approximately as $Re^{0.7}$. An incorrect feature of the computations with Models 3 and 4 at the higher Reynolds number is the shift of the region exhibiting the sudden rise in Nu towards the stagnation point, Fig. 11(b). The origin of this behaviour can be traced to the distribution of turbulent kinetic energy across the near-wall sublayer (a region computed in all cases by the eddy viscosity model). At $Re = 23\,000$, the predicted levels of turbulence energy within the sublayer region shown in Fig. 13(a) grows steadily over the range $1.1 \leqslant r/D \leqslant 1.7$ but they always remain lower than those outside. By contrast, at $Re = 70\,000$ there is an abrupt increase in k within the sublayer between $r/D = 0.8$ and $r/D = 1.1$, Fig. 13(b). Significantly, this is precisely the range over which Nu undergoes its abrupt rise.

Before leaving the case of $H/D = 2.0$, it is of interest to note in Fig. 14 the importance of the additional

† This conjecture is supported by preliminary computations made at UMIST in November 1992 using a second-moment closure across the sublayer.

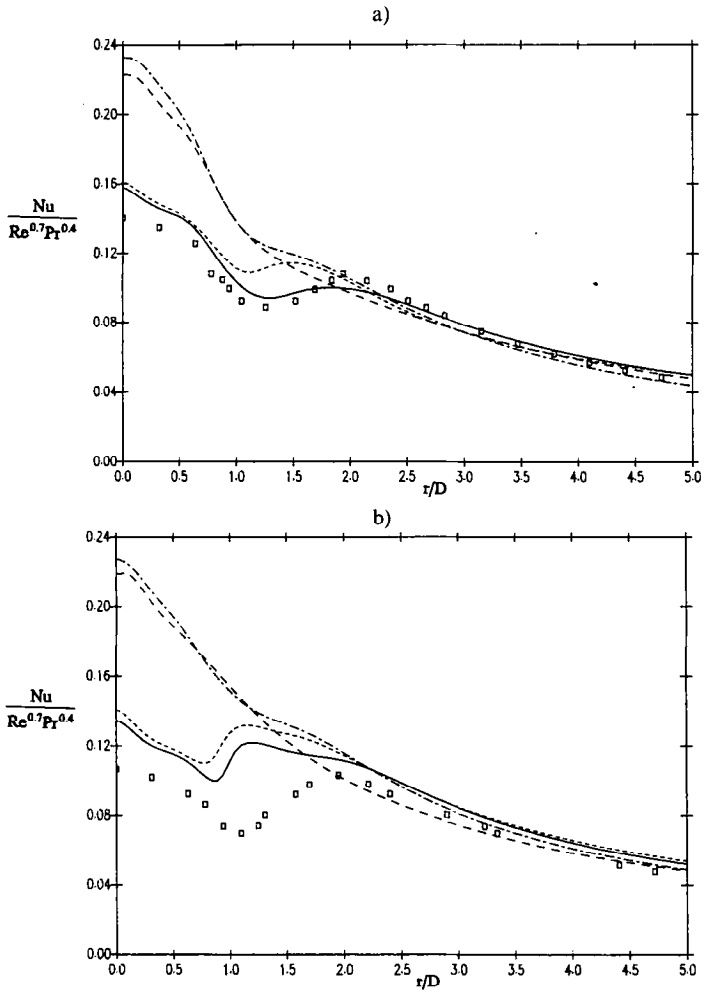

FIG. 11. Variation of scaled Nusselt number with radius. $H/D = 2$. Key as Fig. 2. (a) $Re = 23000$; (b) $Re = 70000$.

term in the ε equation referred to as the 'Yap correction' [11]. The term has only a minor effect on the turbulent velocity and none at all on the mean velocity. Without it, however, the Nusselt number at the stagnation point is nearly twice as high as when it is included. The term achieves its effect through limiting the departure of the near-wall length scale from its equilibrium level, thus raising levels of ε and reducing k. The term is particularly important within the region covered by the k–ε model. As one proceeds to larger radii and the near-wall profiles of k and ε revert towards those found in a uniform-stress shear flow, the effect of the term becomes negligible.

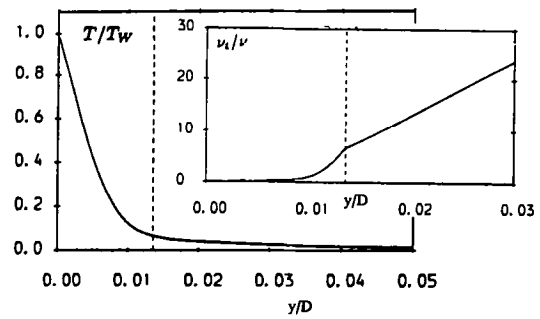

FIG. 12. Mean temperature and effective turbulent viscosity profiles near impingement point. $H/D = 2.0$; $Re = 23000$. Computations using Model 4.

The Nusselt number predictions for $H/D = 6.0$ appear in Fig. 15. There are several points to note. While Models 1 and 2 still achieve the worst agreement, it is significant that the second moment closure now gives results inferior to those of the eddy viscosity scheme. The reason is that near-wall turbulent energies along the symmetry line are now much higher than for $H/D = 2.0$, so the erroneous action of ϕ_{ij2}^{w} to increase velocity fluctuations normal to the wall creates greater anomalies. Model 2 also stands out as the only scheme giving *too low* levels of Nu for $r/D > 4.0$. The reason for this is directly linked to the excessive levels of Nu near the stagnation point. Imagine the wall is heated, so the excessive heat transfer coefficients near the stagnation point means that

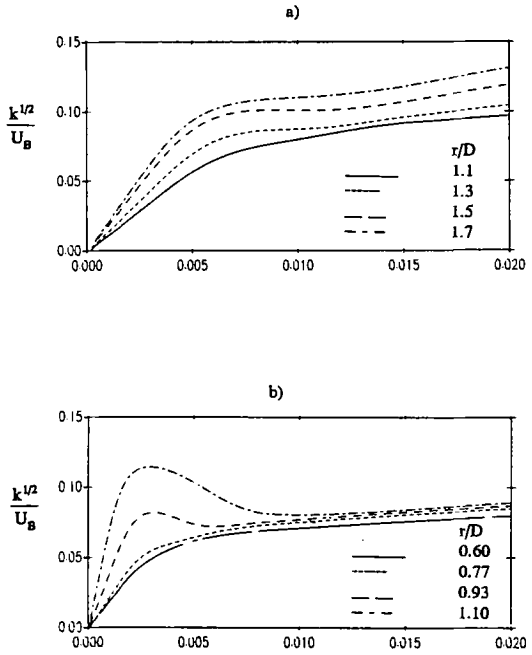

FIG. 13. Computed turbulent energy profiles in near-wall region.

the enthalpy thickness of the thermal boundary layer becomes too large; this in turn leads to mean temperature gradients across the thermal layer becoming too low. At larger radii, as the excessive levels of turbulent diffusivities disappear, the too low temperature gradients produce too low heat transfer coefficients.

Model 3 is now distinctly more successful than Model 4 in predicting heat-transfer coefficients near the stagnation point. Even for Model 3 there are nevertheless fairly serious discrepancies with the experimental data: an overestimate of Nu at the stagnation point of some 25% at $Re = 23\,000$ increasing to 35% at $Re = 70\,000$. In round terms Model 3 gives a Reynolds number exponent at the stagnation point of 0.6 compared with 0.5 indicated by the experiments. Since the variation of v' along the stagnation line is well predicted in the fully turbulent region, the suspicion must be that the problems are arising within the near-wall sublayer where the k–ε model has been adopted. In common with other eddy viscosity models, the scheme adopted here employs the turbulent Reynolds number R_t to dampen the turbulent transport coefficients as the wall is approached. Several workers have commented, however, that the decay of turbulent mixing is due principally to the fact that v' vanishes faster than $k^{1/2}$ as y tends to zero, a phenomenon that is not, to first order, due to viscous effects. Therein would appear to lie the reason for the slightly incorrect dependence of Nu on Reynolds number.

4. CONCLUSIONS

An extensive comparison has been presented of the performance of four transport models of turbulence in predicting the dynamic and thermal characteristics of the near-impingement region of the turbulent impinging jet. Three of the models were of the second-moment closure type that are now beginning to be incorporated into commercial CFD software while the fourth was the widely used k–ε eddy viscosity model. All schemes used a low-Reynolds-number k–ε model across the near-wall semi-viscous sublayer.

Both the eddy viscosity model and the 'basic' Reynolds stress model (Models 1 and 2 respectively) achieved very poor agreement with experiments, the former because of the basic weakness of the eddy viscosity stress–strain relation and the latter due to the incorrect response of its sub-model of the 'wall-reflection' process in a stagnating strain field.

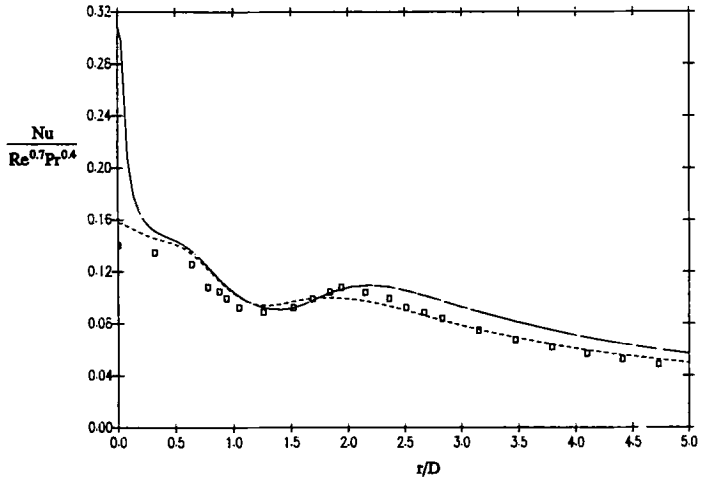

FIG. 14. Effect of Yap correction on Nusselt number. $H/D = 2$; $Re = 23\,000$. --- Model 3; —— Model 3 with Yap correction removed.

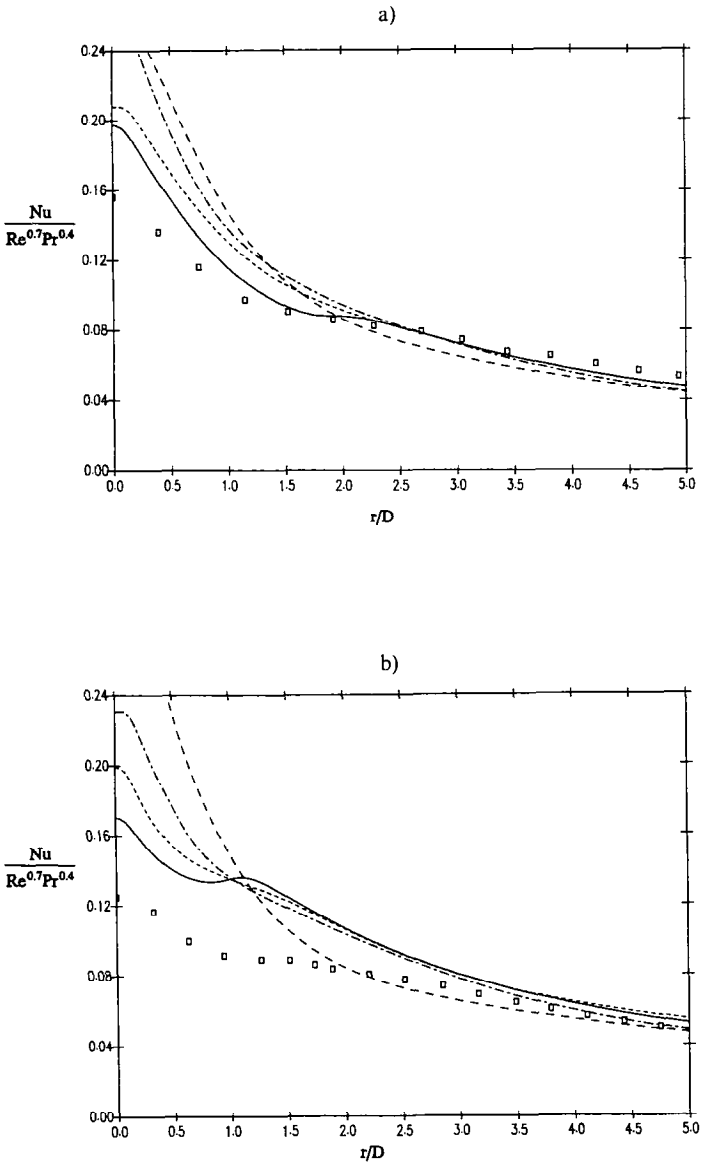

FIG. 15. Variation of normalized Nusselt number with radius. $H/D = 6$. Key as Fig. 2. (a) $Re = 23\,000$; (b) $Re = 70\,000$.

The two other schemes return markedly improved behaviour, particularly Model 3. Since this model simply introduces a replacement wall-reflection model into the basic scheme, it is also attractively simple—at any rate in comparison with Model 4.

Model 3 captures reasonably well the sensitivity of the shape of Nusselt number profile to the height of the impinging jet above the surface, for $r/D < 3.0$. However, the computed variation of Nu on Re at the stagnation point follows a 0.6 power dependence rather than the 0.5 variation of the experiments. It appears that the cause of this discrepancy is to be found in the use of the eddy viscosity model across the sublayer with its excessive reliance on R_t to reduce the turbulent viscosity. Clearly, therefore, the replacement of this model by a low-Reynolds-number second-moment closure is a refinement that should soon be explored.

Acknowledgements—Different phases of this research have been sponsored by the AEA Harwell, CERFACS Toulouse and the SERC through Grant GR/G54740. Dr L. J. W. Graham acknowledges with thanks the receipt of a CSIRO travel scholarship that made his stay at UMIST possible. The manuscript has been assembled for publication by Mrs J. Buckley.

REFERENCES

1. B. E. Launder and B. I. Sharma, *Letters in Heat Mass Transfer* **1**, 131–138 (1974).
2. M. M. Gibson and B. E. Launder, *J. Fluid Mech.* **86**, 491–511 (1978).
3. C. R. Yap, Turbulent heat and momentum transfer in recirculating and impinging flows, Ph.D. Thesis, Faculty of Technology, University of Manchester (1987).

4. T. J. Craft and B. E. Launder, New wall-reflection model applied to the turbulent impinging jet, *AIAA J.* **30,** 2970–2972 (1992).
5. T. J. Craft, B. E. Launder and D. P. Tselepidakis, *7th Symposium on Turbulent Shear Flows*, Stanford, 1989.
6. T. J. Craft and B. E. Launder, Paper 8-5, *8th Symposium on Turbulent Shear Flows*, Munich, 1991.
7. P. G. Huang and M. A. Leschziner, An introduction and guide to the computer code TEAM, Report TFD/83/9, Thermofluids Division, Department of Mechanical Engineering, UMIST (1983).
8. S. V. Patankar and D. B. Spalding, *Int. J. Heat Mass Transfer* **15,** 1787–1805 (1972).
9. B. Leonard, *Comp. Meth. Appl. Mech. Engng* **19,** 59–98 (1979).
10. T. J. Craft, Second-moment modelling of turbulent scalar transport, Ph.D. Thesis, Faculty of Technology, Univeristy of Manchester (1991).
11. M. A. Leschziner, An introduction and guide to the computer code PASSABLE, Report TFD/82/11, Thermofluids Division, Department of Mechanical Engineering, UMIST (1982).
12. A. R. El Baz, Computational modelling of free turbulent shear flows, Ph.D. Thesis, Faculty of Technology, University of Manchester (1992).
13. D. Cooper, D. C. Jackson, B. E. Launder and G. X. Liao, Impinging jet studies for turbulence model assessment—I. Flow-field experiments, *Int. J. Heat Mass Transfer* **36,** 2675–2684 (1993).
14. J. W. Baughn and S. Shimizu, *ASME J. Heat Transfer* **111,** 1096–1098 (1989).
15. J. W. Baughn, X. J. Yan and M. Mesbah, The effect of Reynolds number on the heat transfer distribution from a flat plate to a turbulent impinging jet, ASME Winter Annual Meeting, November 1992.

APPENDIX

The heat flux and scalar variance equations used with Models 2 and 3 are:

$$\frac{\mathrm{d}\overline{u_i\theta}}{\mathrm{d}t} = d_{i\theta} + P_{i\theta} + \phi_{i\theta} - \varepsilon_{i\theta}$$

$$P_{i\theta} = -\left(\overline{u_iu_k}\frac{\partial T}{\partial x_k} + \overline{u_k\theta}\frac{\partial U_i}{\partial x_k}\right)$$

$$d_{i\theta} = \frac{\partial}{\partial x_l}\left[c_\theta\overline{u_lu_m}\frac{k}{\varepsilon}\frac{\partial\overline{u_i\theta}}{\partial x_m}\right]$$

$$\varepsilon_{i\theta} = 0$$

$$\phi_{i\theta} = -c_{1\theta}\frac{\varepsilon}{k}\overline{u_i\theta} + c_{2\theta}\overline{u_k\theta}\frac{\partial U_i}{\partial x_k}$$

$$\frac{\mathrm{d}\overline{\theta^2}}{\mathrm{d}t} = 2(P_\theta - \varepsilon_\theta) + \mathrm{d}_\theta$$

$$P_\theta = -\overline{u_i\theta}\frac{\partial T}{\partial x_i}$$

$$d_\theta = \frac{\partial}{\partial x_l}\left[c_\theta\overline{u_lu_m}\frac{k}{\varepsilon}\frac{\partial\overline{\theta^2}}{\partial x_m}\right]$$

$$\varepsilon_\theta = 0.5R\overline{\theta^2}\frac{\varepsilon}{k}$$

where the timescale R is taken to be constant and equal to 2.

$$c_{1\theta} = 3.0 \quad c_{2\theta} = 0.5 \quad c_\theta = 0.18$$

When using Model 4, the same heat flux models are used except for:

$$\begin{aligned}\phi_{i\theta} = {} & -1.7[1+1.2(A_2A)^{1/2}]R^{1/2}\frac{\varepsilon}{k}[\overline{u_i\theta}(1+0.6A_2) \\ & -0.8a_{ik}\overline{u_k\theta} + 1.1a_{ik}a_{kj}\overline{u_j\theta}] - 0.2A^{1/2}Rka_{ij}\frac{\partial T}{\partial x_j} \\ & +0.8\overline{u_k\theta}\frac{\partial U_i}{\partial x_k} - 0.2\overline{u_k\theta}\frac{\partial U_k}{\partial x_i} + \frac{1}{3}\frac{\varepsilon}{k}\overline{u_i\theta}\frac{P_{kk}}{2\varepsilon} \\ & -0.4\overline{u_k\theta}a_{il}\left(\frac{\partial U_k}{\partial x_l} + \frac{\partial U_l}{\partial x_k}\right) \\ & +0.1\overline{u_k\theta}a_{ik}a_{ml}\left(\frac{\partial U_m}{\partial x_l} + \frac{\partial U_l}{\partial x_m}\right) \\ & -0.1\overline{u_k\theta}(a_{im}P_{mk} + 2a_{mk}P_{im})/k \\ & +0.15a_{ml}\left(\frac{\partial U_k}{\partial x_l} + \frac{\partial U_l}{\partial x_k}\right)(a_{mk}\overline{u_i\theta} - a_{ml}\overline{u_k\theta}) \\ & -0.05a_{ml}\left[7a_{mk}\left(\overline{u_i\theta}\frac{\partial U_k}{\partial x_l} + \overline{u_k\theta}\frac{\partial U_i}{\partial x_l}\right)\right. \\ & \left.-\overline{u_k\theta}\left(a_{ml}\frac{\partial U_i}{\partial x_k} + a_{mk}\frac{\partial U_i}{\partial x_l}\right)\right]\end{aligned}$$

The scalar variance dissipation rate is obtained from the transport equation:

$$\begin{aligned}\frac{\mathrm{d}\varepsilon_\theta}{\mathrm{d}t} = {} & -\left(2\frac{\varepsilon_\theta^2}{\overline{\theta^2}} + 0.92\frac{\varepsilon\varepsilon_\theta}{k}\right)\left(\frac{1}{1+0.5A_2^{1/2}A}\right) + \frac{1.6}{R}\frac{\varepsilon}{k}P_\theta \\ & + \frac{2.6}{R}\nu_t\frac{\varepsilon_\theta}{k}\left(\frac{\partial U_i}{\partial x_j}\right)^2 + \frac{\partial}{\partial x_l}\left[c_\theta\overline{u_lu_m}\frac{k}{\varepsilon}\frac{\partial\varepsilon_\theta}{\partial x_m}\right]\end{aligned}$$

$$\nu_t = c_\mu k^2/\varepsilon$$

$$c_\theta = 0.18 \quad c_\mu = 0.09$$